Inorganic Chemistry
Article

Inorg. Chem. **2009**, *48*, 11251–11258 **11251**
DOI: 10.1021/ic901752w

Syntheses, Characterization, and Computational Study of WSF_4 and $WSF_4 \cdot CH_3CN$

Jared Nieboer,[†] William Hillary,[†] Xin Yu,[†] Hélène P. A. Mercier,[‡] and Michael Gerken*[,†]

[†]*Department of Chemistry and Biochemistry, The University of Lethbridge, Lethbridge, Alberta T1K 3M4, Canada, and* [‡]*Department of Chemistry, McMaster University, Hamilton, Ontario L8S 4M1, Canada*

Received September 3, 2009

A new and improved synthetic route to WSF_4 was developed from the reaction of WF_6 and Sb_2S_3 in anhydrous HF. Tungsten sulfide tetrafluoride was characterized by Raman and ^{19}F NMR spectroscopy for the first time in HF solvent. Both studies provided evidence for its monomeric form in HF solution. In the solid state, WSF_4 was also characterized by Raman and infrared spectroscopy. The $WSF_4 \cdot CH_3CN$ adduct was prepared from WSF_4 and CH_3CN in anhydrous HF solvent and by the direct combination of WSF_4 with excess CH_3CN, and was characterized by Raman and infrared spectroscopy in the solid state and ^{19}F NMR spectroscopy in CH_3CN solution. The crystal structure of $WSF_4 \cdot CH_3CN$ was obtained and showed that CH_3CN coordinates to W in an end-on fashion and trans to the W−S bond. Quantum-chemical calculations using B3LYP and PBE1PBE methods were used to calculate the gas-phase geometries and vibrational frequencies of WSF_4 and $WSF_4 \cdot CH_3CN$.

Introduction

Although oxide fluorides of transition metals have attracted considerable attention,[1] reports related to the analogous high-oxidation-state sulfide fluorides have been scarce. Among all transition-metal sulfide fluorides, WSF_4 has been the most studied system. Tungsten sulfide tetrafluoride has been characterized by electron-diffraction in the gas-phase;[2] by EXAFS[3] and ^{19}F NMR spectroscopy[4] in solution; and in the solid state by Raman and infrared spectroscopy,[4] and X-ray crystallography.[5] While WSF_4 was found to be monomeric in the gas-phase[2] and in CH_3CN and CH_2Cl_2 solutions,[3] it was found to adopt a fluorine-bridged chain structure in the solid state.[5]

The primary synthetic route to WSF_4 has been the solid state substitution of two fluorine ligands in WF_6 by a sulfur ligand using high-temperature reactions and reagents such as Sb_2S_3 (300 °C),[4] B_2S_3 (260 °C), and sulfur (300 °C),[5] followed by purification of WSF_4 by vacuum sublimation.[2] A solution synthesis utilizing $S(Si(CH_3)_3)_2$ in CH_3CN and CH_2Cl_2 solvents (eq 1) has also been reported.[3] However, variable amounts of a dark brown solid were obtained as a side product. A solvent-assisted dismutation of WSF_4 in CH_3CN was suggested resulting in the formation of WF_6 and WS_3 according to eq 2.

$$WF_6 + S(Si(CH_3)_3)_2 \xrightarrow{CH_3CN \text{ or } CH_2Cl_2} WSF_4 + FSi(CH_3)_3 \quad (1)$$

$$3WSF_4 \xrightarrow{CH_3CN} 2WF_6 + WS_3 \quad (2)$$

In spite of these studies, a facile, high-yield synthetic route to pure WSF_4 is still missing. This is primarily a consequence of side-reactions resulting in a dark brown solid that is presumed to be WS_3. In addition, WSF_4 was found to be photosensitive, changing its color to pale brown upon exposure to direct sunlight.[4]

The solubility of WSF_4 in CH_3CN suggested the possible formation of a $WSF_4 \cdot CH_3CN$ adduct.[5] Preliminary crystallographic data confirmed adduct formation; however, the data quality was insufficient to determine the correct space group and to provide detailed structural information.

The goal of this study is to provide a reliable and facile high-yield synthesis of pure WSF_4 and $WSF_4 \cdot CH_3CN$, and their full structural characterizations.

Results and Discussion

Synthesis of WSF_4. Pure WSF_4 was synthesized from WF_6 and Sb_2S_3 in anhydrous HF (aHF) solvent at room temperature with an approach analogous to that used for $ReSF_4$ (eq 3).[6]

$$3WF_{6(HF)} + Sb_2S_{3(s)} \xrightarrow{HF,\ 14\ h} 3WSF_{4(HF)} + 2SbF_{3(s)} \quad (3)$$

*To whom correspondence should be addressed. E-mail: michael.gerken@uleth.ca.

(1) Gerken, M.; Mercier, H. P. A.; Schrobilgen, G. J. In *Advanced Inorganic Fluorides*; Nakajima, T.; Žemva, B.; Tressaud, A., Eds.; Elsevier Science: Amsterdam, 2000; pp 117−174.
(2) Rice, D. A.; Hagen, K.; Hedberg, L.; Hedberg, K.; Staunton, G. M.; Holloway, J. H. *Inorg. Chem.* **1984**, *23*, 1826–1828.
(3) Banger, K. K.; Blackmann, C. S.; Brisdon, A. K. *J. Chem. Soc., Dalton Trans.* **1996**, 2975–2978.
(4) Atherton, M. J.; Holloway, J. H. *Chem. Commun.* **1977**, 424–425.
(5) Holloway, J. H.; Kaučič, V.; Russell, D. R. *Chem. Commun.* **1983**, 1079–1081.

Published on Web 10/27/2009

The reaction proceeded slowly at room temperature, yielding a stable yellow HF solution above insoluble SbF_3 and incompletely reacted antimony sulfide fluorides. Decantation of the supernatant followed by the removal of all volatiles under vacuum yielded yellow WSF_4. The solubility of isolated solid WSF_4 in aHF solvent was somewhat less than that of WSF_4 that was generated in solution, suggesting the presence of monomeric WSF_4 in HF solvent and the formation of fluorine-bridged chains in the solid state. It was found that solid WSF_4 changes color from yellow to brown after a day at room temperature in the absence of light. Maintaining the sample at low temperature (below −10 °C) prevented the color change. The color change is possibly the result of (a) slow decomposition or (b) particle coagulation over a period of time that results in the formation of larger aggregates. Although fluorescence of freshly prepared WSF_4 was minimal in the Raman spectrum, a marked increase in fluorescence was observed for older samples. Because the reactivity of brown WSF_4 samples that were stored at room temperature for extended periods of time did not differ from freshly prepared samples, decomposition of the bulk sample seems an unlikely cause of the color change.

Synthesis of $WSF_4 \cdot CH_3CN$. The $WSF_4 \cdot CH_3CN$ adduct was synthesized by the reaction of freshly prepared WSF_4 with CH_3CN in aHF solvent below −20 °C (eq 4) and by the reaction of solid WSF_4 with neat CH_3CN solvent at −40 °C (eq 4). Crystallization of $WSF_4 \cdot CH_3CN$ from aHF gave $WSF_4 \cdot CH_3CN$ in high purity as bright yellow needles. The reaction in neat CH_3CN initially produced a red-brown solution, yielding a gray solid upon removal of all volatiles. The $WSF_4 \cdot CH_3CN$ adduct is stable at room temperature under anhydrous conditions and can be used as a stable synthetic susbstitute for WSF_4. The $WSF_4 \cdot CH_3CN$ adduct is moderately soluble in CH_2Cl_2.

$$WSF_4 + CH_3CN \xrightarrow{\text{aHF or } CH_3CN} WSF_4 \cdot CH_3CN \quad (4)$$

Vibrational Spectroscopy. (a). WSF_4. The Raman spectrum of a solution of WSF_4 in aHF solvent is shown in Figure 1, and the Raman and infrared spectra of solid WSF_4 are shown in Figure 2. The observed Raman frequencies of WSF_4 in HF solution and their detailed assignments are summarized in Table 1 together with the calculated vibrational frequencies for monomeric WSF_4. The observed vibrational frequencies of solid WSF_4 are listed in Table 2 along with their general assignments. Overall, there is better agreement between experimental and calculated data using the B3LYP method.

The Raman spectrum of an aHF solution of WSF_4 is in agreement with monomeric WSF_4 having C_{4v} symmetry as predicted by computational studies and indicated in a previous EXAFS study in CH_3CN and CH_2Cl_2 solvents and a gas-phase electron-diffraction study.[2,3] The vibrations of monomeric WSF_4 span the irreducible representations $\Gamma = 3A_1 + 2B_1 + B_2 + 3E$ under C_{4v} symmetry. All vibrational modes are Raman active, while the A_1 and E modes are infrared active.

The band observed at 690 cm^{-1} is attributable to the $\nu_s(WF_4)$ mode. The $\nu_{as}(WF_4)$ modes, $\nu_7(E)$ and $\nu_4(B_1)$, are

(6) Holloway, J. H.; Puddick, D. C.; Stounton, G. M.; Brown, D. *Inorg. Chim. Acta* **1982**, *64*, L209–210.

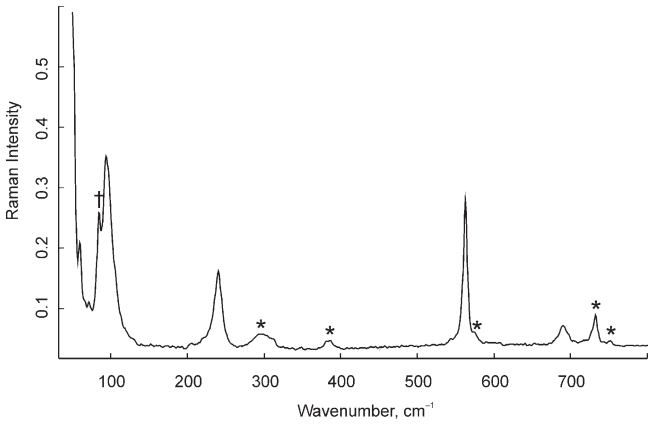

Figure 1. Raman spectrum of an aHF solution of WSF_4 in a FEP tube recorded at −15 °C using 1064 nm excitation. Asterisks (*) and dagger (†) denote FEP bands and a laser line, respectively.

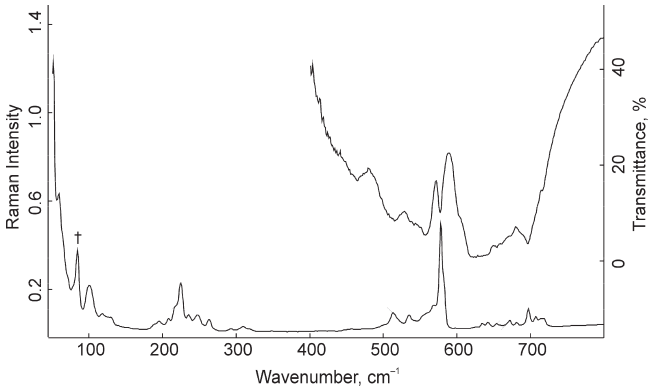

Figure 2. Vibrational spectra of WSF_4: Raman spectrum (lower trace) recorded at −100 °C using 1064 nm excitation and the infrared spectrum (upper trace) recorded at room temperature in a KBr pellet. The dagger (†) denotes a laser line.

calculated to be weaker and were not observed in the Raman spectrum. The value reported for matrix-isolated WSF_4, 671 cm^{-1},[10] is, however, in agreement with the calculated value for $\nu_7(E)$. As predicted by the calculations, the W−S stretching mode appears as the most intense band in the Raman spectrum at 563 cm^{-1}. Another, weaker band is observed at 544 cm^{-1} and has been assigned to the $\nu(W-^{34}S)$ mode by analogy with the $WSF_4 \cdot CH_3CN$ adduct (vide infra). A similar isotopic effect on the W−S stretching frequency was observed for matrix-isolated WSF_4.[10] The bands at 303, 313 cm^{-1} are assigned to $\delta_{scissoring}(WF_4)$ and that at 241 cm^{-1} is assigned to $\delta(SWF)$, based on its relative intensity. The absence of bands in the $W-F_{bridging}$ stretching region between 500 and 540 cm^{-1} confirms the monomeric structure of WSF_4 in HF solution.

The Raman spectrum of pure solid WSF_4 is more complex, reflecting the polymeric nature of WSF_4 in the solid state. The present infrared values are in agreement with those reported earlier.[4] Previously, only one Raman band had been reported at 577 cm^{-1}, which was attributed to the W−S stretching mode. The nine bands between 635 and 718 cm^{-1}, and the five bands between 554 and 585 cm^{-1}, observed in the present study, can be attributed to $W-F_t$ and W−S stretching modes, respectively, by analogy with those observed for monomeric

Table 1. Experimental Raman Frequencies and Assignments for WSF_4 Dissolved in aHF and Calculated Vibrational Frequencies for Monomeric WSF_4

exptl[a,b]		calcd[a,c]				
WSF_4		$W^{32}SF_4$		$W^{34}SF_4$		
Raman[d]	matrix[e]	B3LYP	PBE1PBE	B3LYP	PBE1PBE	assgnt (C_{4v})[f]
690(11)	707	709(13)[91]	729(12)[95]	710(13)[92]	729(11)[95]	$\nu_1(A_1)$, $\nu_s(WF_4)$
	671	680(1)[196]	697(1)[201]	682(1)[196]	697(1)[202]	$\nu_7(E)$, $\nu_{as}(WF_4)$
		624(3)[0]	640(3)[0]	625(3)[0]	640(3)[<0.1]	$\nu_4(B_1)$, $\nu_{as}(WF_4)$
563(77)	577.3	579(28)[47]	598(27)[53]			$\nu_2(A_1)$, $\nu(W^{32}S)$
544(4)	562.9			565(26)[44]	583(26)[50]	$\nu_2(A_1)$, $\nu(W^{34}S)$
313(6)[g]		331(2)[0]	338(2)[0]	331(2)[0]	338(2)[0]	$\nu_6(B_2)$, $\delta_{scissoring}(WF_4)$
303(8)[g]						
		244(1)[5]	247(1)[4]	243(1)[5]	247(1)[4]	$\nu_3(A_1)$, $\delta_{umbrella}(WF_4)$
		235(<1)[19]	238(<1)[19]	235(<1)[18]	238(<1)[19]	$\nu_8(E)$, $\delta_{in\text{-}plane}(WF_4)$
241(40)		206(4)[0]	208(3)[0]	203(3)[<0.1]	205(3)[<0.1]	$\nu_9(E)$, $\delta(SWF)$
		122(<1)[0]	123(<1)[0]	120(<1)[0]	123(<1)[0]	$\nu_5(B_1)$, $\delta_{out\text{-}of\text{-}plane}(WF_4)$
94(100)						modes associated with solvation
72(24)						
60(54)						

[a] Frequencies are given in cm^{-1}. [b] Values in parentheses denote relative Raman intensities. [c] Stuttgart f (W) and aug-cc-pVTZ (H,C,N,O,F,S) basis sets. Values in parentheses denote Raman intensities ($Å^4\ u^{-1}$). Values in square brackets denote infrared intensities (km mol^{-1}). Values in parentheses denote relative Raman intensities. [d] The Raman spectrum of WSF_4 dissolved in aHF was recorded in an FEP sample tube at −15 °C using 1064 nm excitation. FEP bands were observed at 293(6), 382(4), 386(4), 574sh, 733(16), 752(3) cm^{-1}; a laser line was observed at 85 cm^{-1}. [e] Values from ref 10 in a nitrogen-matrix. [f] The abbreviations denote symmetric (s), asymmetric (as), stretch (ν), bend (δ), and rock (ρ_{rock}). The in-plane and out-of-plane mode descriptions are relative to the WF_4 plane. [g] These bands overlap with the FEP band at 293 cm^{-1}.

Table 2. Experimental Vibrational Frequencies[a] and Assignments for Solid WSF_4

Raman[b,c]	infrared[b,d]	infrared[b,e]	assgnt
718(8)			
715(8)	716 sh		
707(10)			
697(18)	695 s	699	
681(4)			$\nu(W\text{–}F_{term})$
672(7)	675 sh	673	
654(4)			
642(5)		643	
635(4)	630 vs		
585sh			
578(100)	576 s	577	
568(23)			$\nu(W\text{–}S)$
560sh			
554sh	556 s		
535(13)	538 sh	534	
513(17)	514 s	514	$\nu(W\text{–}F_{bridge})$
473(2)	463 m		
457(2)			
319sh			
309(4)			
293(2)			
263(10)			
248(14)			
236(14)			
225(44)			
218sh			
208(10)			
195(8)			
190sh			
130(6)			
118(5)			
101(26)			
59(74)			

[a] Frequencies are given in cm^{-1}. [b] Abbreviations denotes shoulder (sh), very strong (vs), strong (s), medium (m), weak (w), very weak (vw). [c] The Raman spectrum of solid WSF_4 was recorded in a sealed mp capillary at −100 °C using 1064-nm excitation. A laser line was observed at 84 cm^{-1}. [d] The infrared spectrum of WSF_4 was recorded on a KBr pellet at room temperature. [e] Values from ref 4.

WSF_4. The most intense Raman band at 578 cm^{-1} occurs 15 cm^{-1} higher than that of WSF_4 in solution which is counterintuitive because monomeric WSF_4 should exhibit more covalent W−S bonding when compared with a fluorine-bridged chain. However, vibrational coupling in the fluorine-bridge chain can easily result in a high-frequency shift of a W−S stretching band. The modes around 473 and 513 cm^{-1} in the Raman spectrum (463 and 514 cm^{-1} in the infrared spectrum) do not appear in the solution spectrum and are confidently assigned to the $W-F_b$ stretching modes. Such modes are indeed expected in view of the chain structure found by X-ray crystallography. The modes observed below 319 cm^{-1} are all associated to deformation modes which are likely strongly coupled because of the chain structure of WSF_4. The intense Raman band at 225 cm^{-1} can tentatively be assigned to δ(SWF) in comparison with the Raman spectrum of WSF_4 in HF solvent.

The $W-F_t$ stretching modes for solid WSF_4 appear at lower frequency than those in WOF_4 (660 and 725 cm^{-1})[8] which adopts a fluorine-bridged tetrameric structure in the solid state,[7] in agreement with the greater electronegativity of oxygen, which is expected to result in an electron-poorer tungsten center and a more covalent W−F bond. The $W-F_b$ stretches in WSF_4 appear at even lower frequency than those in WOF_4 (520 and 560 cm^{-1}), indicating much weaker fluorine bridging in WSF_4.

(b). $WSF_4 \cdot CH_3CN$. The Raman and infrared spectra of $WSF_4 \cdot CH_3CN$ are shown in Figure 3. The observed vibrational frequencies of $WSF_4 \cdot CH_3CN$, their assignments, and the calculated frequencies are summarized in Table 3. The assignments of the modes are based on the calculated frequencies and Raman intensities of the energy-minimized geometry. Because some of the bands exhibit splittings, a factor-group analysis was carried out (Supporting Information, Table S1).

(7) (a) Edwards, A. J.; Steventon, B. R. *J. Chem. Soc.* (*A*) **1968**, 2503–2510. (b) Alexander, L. E.; Beattie, I. R.; Bukovszky, A.; Jones, P. J.; Marsden, C. J.; Van Schalkwyk, G. J. *J. Chem. Soc., Dalton Trans.* **1974**, 81–84.

(8) Arnaudet, L.; Bougon, R.; Ban, B.; Charpin, P.; Isabey, J.; Lance, M.; Nierlich, M.; Vigner, J. *Inorg. Chem.* **1989**, *28*, 257–262.

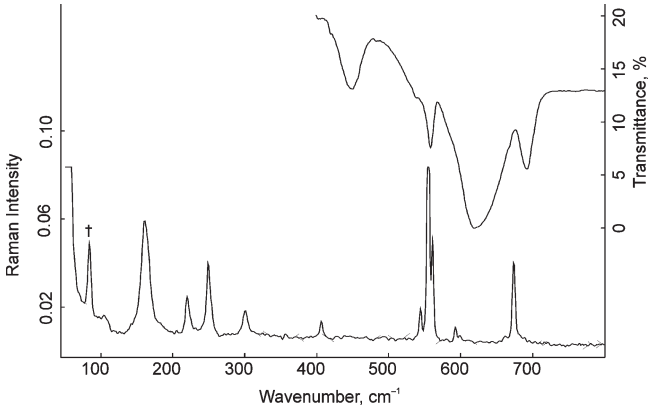

Figure 3. Vibrational spectra of $WSF_4 \cdot CH_3CN$: Raman spectrum (lower trace) recorded at −100 °C using 1064 nm excitation and the infrared spectrum (upper trace) recorded at room temperature in a KBr pellet. The dagger (†) denotes a laser line.

The $WSF_4 \cdot CH_3CN$ adduct in the crystal structure adopts C_s point symmetry (vide infra) with a slightly bent W−N−C moiety. When neglecting the hydrogen atoms of the methyl group, the idealized symmetry of the F_4SWNCC framework is C_{4v} point symmetry, and its vibrational modes span the irreducible representations $\Gamma = 6A_1 + 2B_1 + B_2 + 6E$, all modes being Raman active, while only the A_1 and E modes are infrared active. The vibrational analysis using C_{4v} point symmetry is warranted because no splitting of the experimental and calculated E modes is observed and the lowering of the overall symmetry by the slight deviation from linearity of the SWNCC moiety and the presence of the CH_3 group to C_s or lower symmetry does not have a significant influence on the vibrational modes. The symmetry labels for the F_4SWNCC framework under C_{4v} symmetry are given in Table 3.

The vibrational frequencies that are attributable to the CH_3CN ligand all exhibit complexation shifts, compared to free CH_3CN, that are in good agreement with other adducts of CH_3CN and transition metal oxide fluorides, such as $ReO_2F_3 \cdot CH_3CN$.[9] The strong bands observed at 674 and 662 cm^{-1} are assigned to the $\nu_s(WF_4)$ mode, and are significantly lower than that in monomeric WSF_4 in HF solution (690 cm^{-1}) or in the gas-phase (707 cm^{-1}), reflecting the increase in bond polarity upon adduct formation. The infrared band at 619 cm^{-1} is assigned to the doubly degenerate $\nu_{as}(WF_4)$ mode and is very strong, as predicted from the calculations. This band also appears at lower frequency than in WSF_4 in the gas-phase (671 cm^{-1}). The bands at 593 and 599 cm^{-1} are assigned to the $\nu_{as}(WF_4)$ mode of B_1 symmetry. The bands at 544, 555, and 561 cm^{-1} are attributed to W−S stretching modes. Several spectra were recorded for the adduct, and they all revealed the presence of three bands and an invariant intensity ratio, confirming that the band at 561 cm^{-1} is not due to an excess of WSF_4, but originates from vibrational coupling in the crystallographic unit cell, consistent with the factor-group analysis, which predicts the splitting of all Raman modes into two Raman-active components (Supporting Information, Table S1). The strongest band at 555 cm^{-1} is readily assigned to a W−S stretching band, and the band at 544 cm^{-1} is assigned to an isotopic shift resulting from the $W^{34}SF_4 \cdot CH_3CN$ isotopomer. The assignment is confirmed by the experimental shift, 11 cm^{-1}, which is well reproduced by a calculated shift of 14 cm^{-1} at both levels of theory. The W−S stretching frequency is also lower when compared with the W−S stretching frequency (563 cm^{-1}) of monomeric WSF_4. The W−N stretching mode is predicted to occur at very low frequency with a very low intensity, and was consequently not observed. The low frequency reflects the weakness of the coordinate bond. Microcrystalline bulk samples of $WSF_4 \cdot CH_3CN$ that were produced by reactions in HF and CH_3CN solvents frequently contained unidentified impurities that gave rise to broad Raman and infrared bands at 800 cm^{-1}.

NMR Spectroscopy. The solubility of WSF_4 in HF solvent allowed for its study by ^{19}F NMR spectroscopy in that solvent. The ^{19}F NMR spectrum of WSF_4 in HF showed a singlet at 77.4 ppm with satellites due to a $^1J(^{183}W-^{19}F)$ coupling of 42 Hz. The chemical shift is significantly lower than that observed for WSF_4 in the donor solvent CH_3CN (85.4 ppm), which is in good agreement with previously reported values,[3,4] corroborating the formation of the $WSF_4 \cdot CH_3CN$ adduct characterized by Raman spectroscopy and X-ray diffraction. The chemical shift of $WSF_4 \cdot CH_3CN$ dissolved in CH_2Cl_2 exhibited a similar chemical shift at 86.1 ppm; $^1J(^{183}W-^{19}F)$ coupling in CH_2Cl_2 could not be resolved as a consequence of the line width, $\Delta\nu_{1/2} = 21$ Hz. A smaller chemical shift difference between the adduct and the uncomplexed species is observed for WOF_4 (aHF solvent: 60.8 ppm, $^1J(^{183}W-^{19}F) = 68$ Hz; CH_3CN solvent: 66.7 ppm), which was observed in some of the NMR samples as a result of small degree of hydrolysis.

Crystal Structures of WSF_4 and $WSF_4 \cdot CH_3CN$. Details of the data collection parameters and other crystallographic information for WSF_4 and $WSF_4 \cdot CH_3CN$ are given in Table 4 while important bond lengths and bond angles are listed in Table 5.

WSF_4. Although the published structure is crystallographically correct, it was of average quality, with some issues as indicated by the severe distortion of several of the thermal ellipsoids.[5] The present structure of WSF_4 consists of fluorine-bridged chains and contains two crystallographically independent bridged WSF_4 moieties (Figure 4a). The fluorine bridge is asymmetric, with one short bridging W−F_b distance, 1.932(5) and 1.947(5) Å, and one long bridging W---F_b distance, 2.323(4) and 2.308(5) Å. The bridging fluorine forms the long contact trans to the adjacent W=S bond. The *cis*-bridging results in meandering chains that run along the *c*-axis; however, there are no intermolecular contacts between adjacent chains (Figure 4b). The W=S bond lengths in solid WSF_4 (2.084(2) and 2.091(2) Å) are not significantly different from those in the gas-phase, indicating the weakness of the W---F_b bridging contact. The F_t-W---F_b angles are significantly smaller compared to the F_t−W−F_t angles due to the long W---F_b distances. The W−F_b---W angles range from 160.5(2) to 147.0(3)°, indicating the weakness of the fluorine bridge and the flexibility of the angle.

(9) Casteel, W. J.; Dixon, D. A.; LeBlond, N.; Lock, P. E.; Mercier, H. P. A.; Schrobilgen, G. J. *Inorg. Chem.* **1999**, *38*, 2340–2358.
(10) Jones, P. J.; Levason, W.; Ogden, J. S.; Turff, J. W.; Page, E. M.; Rice, D. A. *J. Chem. Soc.; Dalton Trans.* **1983**, 2625–2629.

Table 3. Experimental and Calculated Raman Frequencies and Intensities for $WSF_4 \cdot CH_3CN$ and CH_3CN and Calculated Infrared Intensities for $WSF_4 \cdot CH_3CN$ and CH_3CN

$WSF_4 \cdot CH_3CN$ and CH_3CN

exptl[a]			calcd[a,b]						
$WSF_4 \cdot CH_3CN$		CH_3CN	$W^{32}SF_4 \cdot CH_3CN$ (C_1)		$W^{34}SF_4 \cdot CH_3CN$ (C_1)		CH_3CN (C_{3v})		assgnt {C_{4v}}[f]
Raman[c]	ir[d,e]	Raman	B3LYP	PBE1PBE	B3LYP	PBE1PBE	B3LYP	PBE1PBE	
3019(3)		3001(7)	3124(69)[<1] 3124(69)[<1]	3154(67)[1] 3153(67)[1]	3124(69)[<1] 3124(69)[<1]	3154(67)[1] 3153(67)[1]	3115(59)[<1]	3147(56)[<1]	$\nu_{as}(CH_3)$
2953(34)	2983 vw	2943(100)	3052(256)[<0.1]	3070(256)[<1]	3052(256)[<0.1]	3070(256)[<1]	3048(195)[3]	3067(193)[2]	$\nu_s(CH_3)$
	2916 vw	2888(3)							
	2364 w	2847(2)							
	2343 sh	2732(2)							combination bands
2313(24)	2322 w								
	2308w	2293(5)							
2286(25)	2280 w	2253(60)	2409(228)[88]	2437(229)[98]	2409(228)[88]	2437(229)[98]	2363(81)[11]	2389(80)[13]	$\nu(C\equiv N)$ {$\nu(A_1)$}
	2253 w								
	2217 w	2204(1)							combination bands
	1696 w								
	1580 w								
	1405 m	1443(3)	1468(6)[12]	1457(6)[13]	1468(6)[12]	1457(6)[13]	1475(5)[10]	1465(5)[12]	$\delta_{as}(CH_3)$
		1416(2)	1467(6)[12]	1457(6)[13]	1468(6)[12]	1457(6)[13]			
1364(7)	1367w	1375(6)	1411(12)[1]	1397(10)[2]	1411(12)[1]	1398(10)[2]	1413(6)[2]	1400(6)[3]	$\delta_s(CH_3)$
	1259 m								
	1191 w								combination bands
	1027 m		1062(<1)[3]	1051(<1)[4]	1062(<1)[3]	1051(<1)[4]	1063(<1)[2]	1053(<1)[2]	$\rho_r(CH_3)$
			1062(<1)[3]	1051(<1)[4]	1062(<1)[3]	1051(<1)[4]			
	996 m								combination band
939(5)	935 sh	919(18)	944(7)[13]	968(8)[12]	945(8)[13]	968(8)[12]	928(5)[1]	948(5)[1]	$\nu(C\text{–}CH_3)$ {$\nu(A_1)$}
674(23)									
662 (2)	692 s		685(14)[71]	704(13)[73]	685(14)[73]	704(13)[76]			$\nu_s(WF_4)$ {$\nu(A_1)$}
	619 vs		654(<1)[207]	668(<1)[212]	654(<1)[207]	669(<1)[213]			$\nu_{as}(WF_4)$ {$\nu(E)$}
			654(<1)[207]	668(<1)[212]	654(<1)[207]	669(<1)[213]			
599(2)									
593(4)			607(3)[<0.1]	622(3)[<0.1]	607(3)[<0.1]	622(3)[<0.1]			$\nu_{as}(WF_4)$ {$\nu(B_1)$}
561(29)									
555(100)	558 s		563(51)[103]	580(50)[114]					$\nu(W^{32}S)$ {$\nu(A_1)$}
544(9)	539 sh				549(49)[99]	566(48)[110]			$\nu(W^{34}S)$ {$\nu(A_1)$}
	450 s								combination band
406(4)		380(10)	409(1)[1]	415(1)[1]	409(1)[1]	415(1)[1]	382(1)[<1]	387(1)[<1]	$\delta(CCN)$ {$\nu(E)$}
			409(1)[1]	415(1)[1]	409(2)[1]	415(1)[1]			
301(7)			308(2)[0]	313(2)[0]	307(2)[0]	313(2)[0]			$\delta_{scissoring}(WF_4)$ {$\nu(B_2)$}
			263(<1)[23]	269(<1)[23]	263(<1)[23]	269(<1)[23]			$\delta_{umbrella}(WF_4)$ {$\nu(A_1)$}
249(21)			236(2)[3]	242(2)[4]	235(2)[4]	241(2)[4]			$\delta_{in\text{-}plane}(WF_4)$ {$\nu(E)$}
			236(2)[3]	242(2)[4]	235(2)[4]	241(2)[4]			
220(11)			222(<1)[14]	223(<1)[14]	221(<1)[13]	222(<1)[13]			$\delta(SWF_4)$ {$\nu(E)$}
			222(<1)[14]	223(<1)[14]	221(<1)[13]	222(<1)[13]			
			180(<1)[<0.1]	185(<1)[<0.1]	181(<1)[<0.1]	185(<1)[<0.1]			$\delta_{out\text{-}of\text{-}plane}(WF_4)$ {$\nu(B_1)$}
161(32)			147(3)[<0.1]	152(3)[<0.1]	146(3)[<0.1]	151(3)[<0.1]			$\delta(SWN)$ {$\nu(E)$}
			147(3)[<0.1]	152(3)[<0.1]	146(3)[<0.1]	151(3)[<0.1]			
			140(<1)[15]	153(<1)[16]	140(<1)[5]	153(<1)[16]			$\nu(WN)$ {$\nu(A_1)$}
			37(<0.1)[4]	38(<0.1)[4]	37(<0.1)[5]	38(<0.1)[4]			$\rho_t(CH_3)$
			37(<0.1)[4]	38(<0.1)[4]	37(<0.1)[5]	38(<0.1)[4]			
			10(0)[<0.1]	24(0)[<0.1]	5(<0.1)[<0.1]	24(0)[<0.1]			$\rho_t(CH_3)$
104 (3)									lattice mode

[a] Frequencies are given in cm^{-1}. [b] Stuttgart f (W) and aug-cc-pVTZ (H,C,N,O,F,S) basis sets. Values in parentheses denote Raman intensities ($Å^4\ u^{-1}$). Values in square brackets denote infrared intensities (km mol^{-1}). [c] The Raman spectrum of $WSF_4 \cdot CH_3CN$ was recorded in a sealed mp capillary at −100 °C using 1064 nm excitation. Values in parentheses denote relative Raman intensities. [d] The infrared spectrum of $WSF_4 \cdot CH_3CN$ was recorded on a KBr pellet at ambient temperature; broad. [e] Broad infrared band at 885 from unidentified impurity. [f] The abbreviations denote symmetric (s), asymmetric (as), stretch (ν), bend (δ), and rock (ρ_{rock}). The in-plane and out-of-plane mode descriptions are relative to the WF_4 plane.

Table 4. Crystallographic Data for WSF_4 and $WSF_4 \cdot CH_3CN$

chem formula	WSF_4	$WSF_4 \cdot CH_3CN$
space group	$Pca2_1$ (No. 29)	*Pnma* (No. 62)
a (pm)	16.886(3)	1099.5(3)
b (pm)	5.3754(8)	787.4(3)
c (pm)	9.4435(14)	804.6(2)
molecules/unit cell	8	4
mol wt (g mol^{-1})	291.91	332.96
calcd density (g cm^{-3})	4.524	3.175
T (°C)	−120	−120
μ (mm^{-1})	27.381	16.87
R_1[a]	0.0201	0.0123
wR_2[b]	0.0412	0.0301

[a] R_1 is defined as $\sum||F_o| - |F_c||/\sum|F_o|$ for $I > 2\sigma(I)$. [b] wR_2 is defined as $[\sum w(F_o^2 - F_c^2)^2/\sum w(F_o^2)^2]^{1/2}$ for $I > 2\sigma(I)$.

$WSF_4 \cdot CH_3CN$. The $WSF_4 \cdot CH_3CN$ adduct crystallizes in the orthorhombic space group *Pnma*. The data quality in a previous study was insufficient to distinguish between the $Pna2_1$ or *Pnam* (conventional space group, *Pnma*) space groups.[5] In the crystal structure (Figure 5a), the $WSF_4 \cdot CH_3CN$ adduct is located on a crystallographic mirror plane and the CH_3CN ligand is coordinated to tungsten trans to the sulfur with an essentially linear S−W---N arrangement and a slightly bent W---N−C geometry (174.6(3)°). The W---N distance is rather long, implying rather weak coordination, in agreement with the small complexation shift observed for the ν(CN) mode in the adduct compared to that of free CH_3CN.

The W−S bond length (2.0959(11) Å) is slightly elongated or equal within $\pm 3\sigma$ when compared with the W−S bond lengths of solid WSF_4 (2.084(2) and 2.091(2) Å); the elongation reflects the greater Lewis basicity of N in CH_3CN compared to the "fluoride ion" of the bridge in solid WSF_4. A similar trend is observed between the $W-F_t$ bond lengths in $WSF_4 \cdot CH_3CN$ (1.856(2) and 1.857(2) Å) and the $W-F_t$ bonds in WSF_4 (1.835(5) and 1.852(4) Å). Both the W−S and $W-F_t$ bond lengths are comparable to those in the gas-phase.[2] The S−W−F angles with 100.74(6) and 100.12(6)° are significantly greater than 90° as a consequence of the greater steric demand of the sulfide group relative to that of the weakly coordinated CH_3CN ligand.

Computational Results. The electronic structures of WSF_4 and $WSF_4 \cdot CH_3CN$ were optimized under C_{4v}

Table 5. Experimental and Calculated Metric Parameters for WSF_4 and $WSF_4 \cdot CH_3CN$

	WSF_4					$WSF_4 \cdot CH_3CN$		
	exptl (polymeric)	exptl (monomeric)		calcd (monomeric)		exptl	calcd	
	X-ray	gas-phase[a]	EXAFS[b]	B3LYP[c]	PBE1PBE[c]	X-ray	B3LYP[c]	PBE1PBE[c]
				Bond Lengths (Å)				
W−F_t	1.835(5) to 1.852(4)	1.847(3)	1.863(3)	1.859	1.845	1.8564(15),1.8572(17)	1.871	1.857
W−F_b	1.932(5), 1.947(5)							
W---F_b	2.308(5), 2.323(4)							
W−S	2.084(2), 2.091(2)	2.104(7)	2.026(8)	2.108	2.094	2.0959(11)	2.120	2.107
W---N						2.369(3)	2.494	2.450
N−C1						1.130(5)	1.144	1.143
C1−C2						1.453(5)	1.450	1.444
				Bond Angles (deg)				
S−W−F_t	101.37(18) to 102.59(19)	104.5(11)		105.5	105.7	100.74(6), 100.12(6)	101.7	101.8
S−W---F_b	177.86(15), 177.93(15)							
S−W−F_b	99.48(16), 99.86(16)							
F_t−W−F_t	84.0(2) to 91.9(2)	86.6(5)	85.9	85.8		87.99(11), 88.30(14)	87.6	87.6
	155.0(2) to 158.8(2)		148.9	148.6		155.0(2), 158.8(2)	156.5	156.3
cis-F_t−W−F_b	83.9(2) to 85.1(2)							
F_t−W---F_b	77.2(2) to 80.1(2)							
F_b−W---F_b	78.07(19), 78.89(18)							
W−F_b---W	160.5(2), 147.0(3)							
S−W---N						179.32(9)	180	180
F_t−W---N						79.39(8), 79.74(8)	78.3	78.2
W---N−C						174.6(3)	179.6	179.9
N−C−C						179.0(4)	180	180

[a] Values from ref 2. [b] Values from ref 3. [c] Stuttgart f (W) and aug-cc-pVTZ (H,C,N,O,F,S) basis sets.

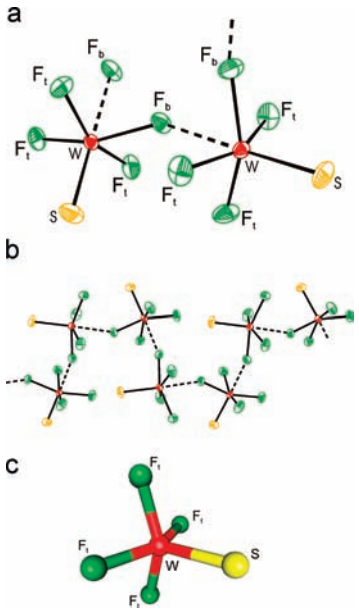

Figure 4. (a) X-ray crystal structure of WSF_4; thermal ellipsoids are shown at the 50% probability level. (b) The WSF_4 chain viewed along the *c*-axis. (c) Calculated geometry of monomeric WSF_4.

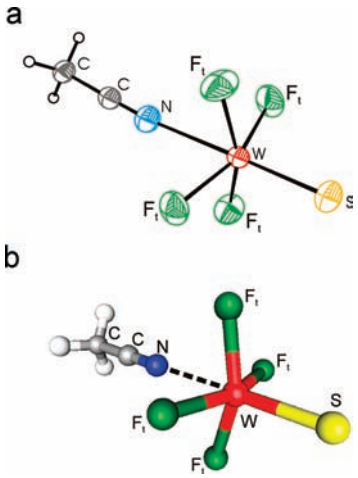

Figure 5. (a) X-ray crystal structure of $WSF_4 \cdot CH_3CN$; thermal ellipsoids are shown at the 50% probability level. (b) The calculated geometry of the $WSF_4 \cdot CH_3CN$ adduct.

symmetry at the B3LYP and PBE1PBE levels and resulted in stationary points with all frequencies real (Figures 4c and 5b). The energy-minimized geometries and vibrational frequencies of WF_6 were also calculated (Supporting Information, Table S2) to serve as a benchmark. The calculated geometrical parameters for WSF_4 and $WSF_4 \cdot CH_3CN$ are listed in Table 5.

The calculated parameters for WSF_4 agree very well with the experimental gas-phase parameters obtained from an electron-diffraction study, and those for $WSF_4 \cdot CH_3CN$ agree well with the present experimental structure. As expected, the largest discrepancy occurs for the W···N contact, which is overestimated at both levels.

Conclusions

Pure WSF_4 can be prepared by means of a facile synthetic route in aHF solvent. Solutions of WSF_4 in aHF were studied for the first time and were shown to contain monomeric C_{4v}-symmetric WSF_4. The $WSF_4 \cdot CH_3CN$ adduct was formed in the donor-solvent CH_3CN and in aHF solvent in the presence of CH_3CN. For the first time, the $WSF_4 \cdot CH_3CN$ adduct could be unambiguously characterized by vibrational spectroscopy in

conjunction with quantum-chemical calculations and X-ray diffraction. The $WSF_4 \cdot CH_3CN$ adduct can serve as the synthetic equivalent to monomeric WSF_4, with its reactivity currently under investigation in our laboratory.

Experimental Section

Materials and Apparatus. All volatile materials were handled (a) on a Pyrex vacuum line equipped with glass/Teflon J. Young valves and (b) a vacuum line constructed of nickel, stainless steel, and FEP. Nonvolatile materials were handled in the dry nitrogen atmosphere of a drybox (Omni Lab, Vacuum Atmospheres). Reaction vessels and NMR sample tubes were fabricated from ¼ in. o.d. thin-wall (3/16 in. i.d.) and 4 mm o.d., 2.8 mm i.d. FEP tubing, respectively, and outfitted with Kel-F valves. All reaction vessels and sample tubes were rigorously dried under dynamic vacuum prior to passivation with 1 atm of F_2 gas.

Anhydrous HF (Air Products, 99.9%) was dried over K_2NiF_6. The solvents, CH_3CN (Sigma-Aldrich, HPLC grade) was dried according to standard literature methods[11] and CH_2Cl_2 was dried using molecular sieves (type 4 Å). Tungsten hexafluoride (Elf Atochem) was used without further purification, whereas Sb_2S_3 (Alfa Aesar, 99.5%) was purified by drying under dynamic vacuum at 160 °C for about 6 h.

Preparation of WSF_4. Inside the drybox, dried Sb_2S_3 (0.136 g, 0.400 mmol) was added to a ¼ in. FEP T-reactor equipped with a Kel/F valve. After distillation of 1.76 g of aHF, WF_6 (0.326 g, 1.09 mmol) was condensed onto the frozen reaction mixture at −196 °C. The reactor was backfilled with dry $N_{2(g)}$ and allowed to warm to room temperature. After warming to room temperature, and with intermittent agitation over the course of 16 h, the reaction progressed slowly, going from a colorless solution above black Sb_2S_3 to a deep yellow solution. The deep yellow solution was decanted to the side arm of the FEP T-reactor where the solution was cooled to about −78 °C causing yellow WSF_4 to precipitate. More WSF_4 was extracted from the solid reaction mixture by condensing HF solvent back onto the solid and washing the solid again at room temperature, followed by decanting the yellow solution into the side arm. The washing procedure was repeated 2 to 3 times. Anhydrous HF was removed under vacuum at −78 °C over several hours, leaving some yellow crystalline material that was pumped on for an additional 10 min at room temperature to ensure total HF removal. The amount of recovered WSF_4 was 0.258 g (0.867 mmol) with a yield of 79.3%.

Preparation of $WSF_4 \cdot CH_3CN$. (**a**) Inside a glovebox, 0.055 g (0.16 mmol) of Sb_2S_3 was transferred into the straight arm of a T-reactor fabricated out of ¼ in. o.d. FEP tubing. After vacuum distillation of about 0.27 mL of aHF onto Sb_2S_3, 0.172 g (0.577 mmol) of WF_6 was condensed onto the Sb_2S_3 at −196 °C by vacuum-distillation. The reaction was allowed to proceed at room temperature overnight, producing a bright yellow solution above a dark gray precipitate. After decanting the solution into the side arm, 0.044 g (1.07 mmol) of CH_3CN was then vacuum-distilled into the side arm at −196 °C. The reaction mixture was vigorously agitated at −35 °C, resulting in a bright yellow solution with some undissolved bright yellow solid. The mixture was then slowly cooled to −61 °C to allow complete precipitation of $WSF_4 \cdot CH_3CN$. The remaining HF was decanted back into the main arm, frozen at −196 °C, and the main arm was heat sealed under dynamic vacuum. Volatiles in the side arm were removed under dynamic vacuum while the cooling bath was allowed to slowly warm to 13 °C. Greenish-yellow $WSF_4 \cdot CH_3CN$ (0.1283 g, 0.3853 mmol) was collected inside the drybox in 79.3% yield. (**b**) Inside a dry nitrogen atmosphere drybox, 0.016 g of WSF_4 (0.055 mmol) was transferred into a ¼ in. thin wall FEP reactor equipped with a Kel-F valve. Approximately 0.35 mL of dry CH_3CN was vacuum distilled onto the solid. Slow melting of the solvent at −43.3 °C resulted in a dark brown solution. After 5 min of agitation, volatiles were removed under dynamic vacuum while the reaction mixture was allowed to slowly warm to −30 °C. Gray-colored $WSF_4 \cdot CH_3CN$ (0.018 g, 0.054 mmol) was recovered in 98% yield.

Vibrational Spectroscopy. The Raman spectra of WSF_4 and $WSF_4 \cdot CH_3CN$ were recorded on a Bruker RFS 100 FT Raman spectrometer with a quartz beam splitter, a liquid-nitrogen-cooled Ge detector, and a low-temperature accessory. The backscattered (180°) radiation was sampled. The actual usable Stokes range was 50 to 3500 cm^{-1} with a spectral resolution of 2 cm^{-1}. The 1064 nm line of an Nd:YAG laser was used for excitation of the sample. All Raman spectra were corrected for effects arising form the optics and the frequency dependence of the Raman scattering by using the white light spectrum of a tungsten lamp. The low-temperature spectra of WSF_4 and $WSF_4 \cdot CH_3CN$ were recorded on a powdered sample in powdered samples in melting point capillaries using laser powers of 150 and 100 mW, respectively. The FT-infrared spectra were recorded on a Nicolet Avatar 360 FTIR spectrometer at ambient temperature. A KBr sandwich was formed in a Wilks minipress inside the drybox by sandwiching the sample between two layers of KBr. The spectra were acquired in 64 scans at a resolution of 2 cm^{-1}.

Nuclear Magnetic Resonance Spectroscopy. All NMR spectra were recorded unlocked on a 300 MHz Bruker Avance II NMR spectrometer equipped with a 5 mm broadband probe. Fluorine-19 (282.404 MHz) NMR spectra were referenced externally to neat $CFCl_3$ at 25 °C. The ^{19}F NMR spectra were typically acquired in 128 K memory with spectral settings of 56 kHz, yielding an acquisition time of 1.15 s and a data point resolution of 0.433 Hz/data point. The number of transients accumulated was 100 using a pulse width of 10.3 μs.

X-ray Crystal Structure Determination of WSF_4 and $WSF_4 \cdot CH_3CN$. (a). Crystal Growth and Crystal Mounting. Crystals of WSF_4 were grown directly from a HF solution upon slow removal of solvent HF at −78 °C under dynamic vacuum. Crystals of $WSF_4 \cdot CH_3CN$ were grown in aHF solvent at a temperature slowly varied from −53 to −59 °C. Crystals of WSF_4 and $WSF_4 \cdot CH_3CN$ having the dimensions $0.10 \times 0.06 \times 0.03\ mm^3$ and $0.55 \times 0.33 \times 0.24\ mm^3$, respectively, were selected at −80 °C for low-temperature X-ray structure determination under a flow of cold nitrogen and mounted as previously described.[12]

(b). Collection and Reduction of X-ray Data. The crystal was centered on a Bruker SMART APEX II diffractometer, equipped with an APEX II 4K CCD area detector and a triple-axis goniometer, controlled by the APEX2 Graphical User Interface (GUI) software,[13] and a sealed source emitting graphite-monochromated Mo Kα radiation (λ = 0.71073 Å). Diffraction data collection at −120 °C consisted of four ω scans at various φ settings of 366 frames each at a fixed χ = 54.74° with a width of 0.5°. The data collection was carried out in a 512×512 pixel mode using 2×2 pixel binning. Processing of the raw data was completed by using the APEX2 software,[13] which applied Lorentz and polarization corrections to three-dimensionally integrated diffraction spots. The program SADABS[14] was used for the scaling of diffraction data, the application of a decay correction, and an empirical absorption correction on the basis of the intensity ratios of redundant reflections.

(c). Solution and Refinement of the Structure. The XPREP program was used to confirm the unit cell dimensions and the

(11) Winfield, J. M. *J. Fluorine Chem.* **1984**, *25*, 91–98.

(12) Gerken, M.; Dixon, D. A.; Schrobilgen, G. J. *Inorg. Chem.* **2000**, *39*, 4244–4255.

(13) *APEX 2*, Version 2.2-0; Bruker AXS Inc.: Madison, WI, 2007.

(14) Sheldrick, G. M. *SADABS*, Version, 2007/4; Bruker AXS Inc.: Madison, WI, 2007.

crystal lattice. The solutions were obtained by direct methods which located the positions of the atoms defining two bridged WSF_4 moieties for WSF_4, and defining WSF_4 and the carbon and nitrogen atoms of the CH_3CN molecules for $WSF_4 \cdot CH_3CN$. The final refinement was obtained by introducing anisotropic thermal parameters and the recommended weightings for all of the atoms. The positions of the hydrogen atoms were calculated. The maximum electron densities in the final difference Fourier map were located near the heavy atoms. All calculations were performed using the SHELXTL-plus package for the structure determination and solution refinement and for the molecular graphics.[15]

Computational Methods. The optimized geometries and frequencies of WF_6, WSF_4, and $WSF_4 \cdot CH_3CN$ were calculated by the density functional theory (DFT) method at the PBE1PBE and B3LYP[16] levels. The Stuttgart basis set augmented by one f-type polarization function (α_f W 0.823)[17] for tungsten and aug-cc-pVTZ basis sets for oxygen, fluorine, nitrogen, carbon, and hydrogen was used. Pseudopotentials were used for tungsten.

Quantum-chemical calculations were carried out using Gaussian 98 and Gaussian 03.[16,18] The levels and basis sets were benchmarked by calculating WF_6 and comparing with the experimental geometries[19] and vibrational frequencies.[20] The geometries were fully optimized using analytical gradient methods. After optimization at one level of theory, the geometries were calculated at the other level of theory to ensure an equivalent energy-minimized geometry had been achieved. The vibrational frequencies were calculated at the PBE1PBE and B3LYP levels using the appropriate minimized geometry, and the vibrational mode descriptions were assigned with the aid of Gaussview.[21]

Acknowledgment. We thank the Natural Sciences and Engineering Research Council of Canada (M.G.), the University of Lethbridge (M.G.), and the Research Corporation (M.G.) for support of this work. The computations were conducted with the aid of the facilities of the Shared Hierarchical Academic Research Computing Network. (SHARCNET: www.Sharcnet.ca)

Supporting Information Available: Factor-group analysis for $WSF_4 \cdot CH_3CN$ (Table S1); benchmark computational study for WF_6 (Table S2); full version of refs 16 and 18; X-ray crystallographic file in CIF format for the structure determination of $WSF_4 \cdot CH_3CN$. This material is available free of charge via the Internet at http://pubs.acs.org.

(15) Sheldrick, G. M. *SHELXTL97*; University of Göttingen: Göttingen, Germany, 1997.
(16) Frisch, M. J.; et al. *Gaussian 03*, revision B.04; Gaussian Inc.: Pittsburgh, PA, 2003.
(17) Ehlers, A. W.; Bohme, M.; Dapprich, S.; Gobbi, A.; Hollwarth, A.; Jonas, V.; Kohler, K. F.; Segmann, R.; Veldkamp, A.; Frenking, G. *Chem. Phys. Lett*. **1993**, *208*, 111–114.
(18) Frisch, M. J. et al *Gaussian 98*, revision A.11; Gaussian Inc.: Pittsburgh, PA, 2003.
(19) Richardson, A.; Hedberg, K.; Lucier, G. M. *Inorg. Chem*. **2000**, *39*, 2787–2793.
(20) Nagarajan, G; Adams, T. S. *Z. Phys. Chem*. **1974**, *255*, 869–888.
(21) *GaussView*, release 3.0; Gaussian Inc.: Pittsburgh, PA, 2003.